Macromolecules

pubs.acs.org/Macromolecules Article

Extreme Deflection of Phase Boundaries and Chain Bridging in A(BA′)$_n$ Miktoarm Star Polymers

Joshua Lequieu, Trenton Koeper, Kris T. Delaney, and Glenn H. Fredrickson*

Cite This: *Macromolecules* 2020, 53, 513−522 Read Online

ACCESS | Metrics & More | Article Recommendations | Supporting Information

ABSTRACT: In this study, we use self-consistent field theory to demonstrate that the A(BA′)$_n$ miktoarm architecture can strongly deflect order−order phase boundaries to large volume fractions f_A. The A(BA′)$_n$ architecture achieves this strong deflection by combining the effects of miktoarm frustration and block bidispersity and is shown to stabilize discrete spheres and cylinders of the A block up to values of $f_A = 0.58$ and $f_A = 0.78$, respectively. We next analyze the prevalence of chain bridging ν_B in both neat miktoarm melts and in homopolymer blends that form the fluctuation-stabilized "bricks and mortar" phase. These calculations demonstrate that high ν_B and f_A can both be simultaneously achieved with highly asymmetric miktoarm stars, a property especially useful for the design of tough thermoplastic elastomers. Finally, we show that these miktoarms exhibit large windows of phase space where the σ and A15 Frank−Kasper phases are stable.

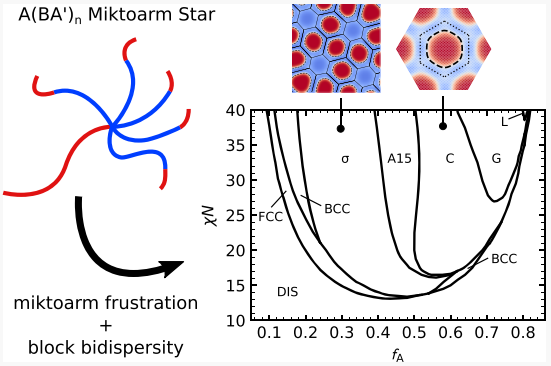

INTRODUCTION

The phase behavior of block polymers is governed by a trade-off between thermodynamic driving forces that seek to minimize both interfacial energy and chain stretching.[1,2] Interfacial energy arises from the chemical incompatibility of different blocks, and favors morphologies that minimize the interfacial area between different domains. This interfacial driving force is balanced by the connectivity of the block polymer and the entropic penalties that arise as the polymer chains stretch to fill space. In linear AB diblock copolymers, the relative importance of interfacial energy and chain stretching is modulated by f_A, the volume fraction of the A block, and χN, where χ is the Flory−Huggins interaction parameter and N is the degree of polymerization.[3,4] Depending on the values of f_A and χN, a linear AB diblock will self-assemble into body-centered cubic (BCC) spheres, hexagonally packed cylinders, double gyroid, and lamella, in addition to small regions of close-packed spheres[5] and the O70 network phase.[6,7] Notably, the values of f_A where these phases are stable are relatively unchanged for many polymer architectures, such as symmetric triblocks (ABA), long alternating (ABABA...), and the (AB)$_n$ star architecture.[8]

For other architectures, the boundaries between different phases can be significantly distorted to different values of f_A. One such architecture is the so-called AB$_n$ miktoarm star, which consists of a single A arm and n B arms that emanate from a single junction.[9,10] In this architecture, the high steric frustration of the B arms favors curvature of the AB interface toward the A domains, which results in the deformation of phase boundaries between ordered phases to larger values of f_A.[8,11,12] The effect of this deformation increases with n, but saturates when $n \approx 4$.[12,13] A similar effect can be observed in conformationally asymmetric linear chains where the A and B blocks have different statistical segment lengths, b_A and b_B where $b_A > b_B$.[11] In this case, the smaller statistical segment length of the B block results in a higher energetic penalty to stretching, which favors curvature of the interface toward the A domains. A notable consequence of the deflection of phase boundaries to larger f_A is the stabilization of new sphere phases, such as the Frank−Kasper phases σ and A15.[12,14−16]

Another approach for deflecting phase boundaries is achieved through asymmetric dispersity of the A and B blocks. Bidispersity in asymmetric triblocks (ABA′) or mixed brushes reduces chain stretching by decreasing the proximity of A monomers to the interface.[17−19] This effect stabilizes interfaces that curve toward the A domains, which leads to the deformation of phase boundaries to larger f_A.[19−22] This effect has been confirmed experimentally for both diblock and triblock copolymers.[23−25]

Though the notion of deflecting phase boundaries may seem somewhat abstract, the ability to stabilize phases at different values of f_A has numerous practical consequences. One compelling example is the case of thermoplastic elastomers (TPEs) where the deflection of phase boundaries can result in

Received: October 25, 2019
Revised: December 23, 2019
Published: January 8, 2020

https://dx.doi.org/10.1021/acs.macromol.9b02254
Macromolecules 2020, 53, 513−522

TPEs that possess a unique combination of hardness, toughness, and elasticity. Typical TPEs are based on the ABA triblock copolymer architecture and consist of a glassy A block (e.g., styrene) and a rubbery B block (e.g., isoprene) that self-assemble into a microphase with discrete A domains. At use temperatures ($T_{g,B} < T \ll T_{g,A}$), the A domains act as physical crosslinks and yield an elastomer, yet at high temperatures ($T > T_{g,A}$), the physical crosslinks fluidize facilitating melt processability. A key requirement in TPEs is that the glassy domains remain discrete (i.e., sphere or cylinder morphologies); if the glassy domains percolate, then elasticity is lost and the materials become plastic.[26] In linear ABA copolymers, this places a restriction that $f_A \lesssim 0.3$,[27] which results in materials that are relatively soft, as the modulus of a TPE typically increases with increasing f_A.[26] In principle, increasing the values of f_A while maintaining discrete A domains should result in a material that is hard, tough, and elastic, which is a unique property combination in unfilled TPEs. The strategies described above to deflect phase boundaries can be used to stabilize sphere and cylinder morphologies at larger values of f_A, thereby providing a route to the this new class of TPE materials.

Recent work by our group[28−33] has made progress toward this goal using $A(BA')_3$ miktoarm star polymers. This design combines the phase boundary deflection resulting from the miktoarm design and block-length bidispersity to deform phase boundaries to larger values of f_A. Initial simulation work indicated that this miktoarm architecture results in exceptional deformation of phase boundaries, and could achieve cylinders of species A at volume fractions of up to $f_A = 0.55$,[28] a prediction that was subsequently confirmed experimentally.[29] Perhaps, most importantly, mechanical tests on these materials indicate that they are indeed strong, tough, and elastic.[29] Polymer alloys consisting of $A(BA')_3$ miktoarm stars and A homopolymers also demonstrate intriguing phase behavior. These alloys have been shown to exhibit highly asymmetric lamellar structures with A volume fractions of 97%,[30] as well as the so-called "bricks and mortar" (B&M) phase,[31] an aperiodic phase consisting of discrete A domains (bricks), surrounded by a continuous B matrix (mortar) that has been shown by field-theoretic simulations (FTS) to be stabilized by fluctuations.[32]

Building on this prior work, in this study, we explore the limits of the miktoarm design to determine the maximum deflection of phase boundaries that can be achieved with the $A(BA')_n$ architecture. Using self-consistent field theory (SCFT), we have found that for a judicious choice of architectural parameters, the miktoarm design can achieve dramatic distortion of the phase diagram, with the sphere phase stable up to $f_A = 0.58$ and cylinders up to $f_A = 0.78$. This exceptional deflection of phase boundaries is achieved through a cooperativity between the steric congestion of the miktoarm design and the bidispersity of the A and A′ blocks. To examine the suitability of these materials for TPEs, we examine the prevalence of chain bridging in both neat miktoarm melts and in polymer alloys that form the B&M phase. We show that the bridging fraction in the cylindrical phase is nearly constant with both f_A and homopolymer volume fraction ϕ_H, respectively, and that bridging fraction increases significantly with n, the number of BA′ arms. This indicates that the deflection of phase boundaries and the connectivity of the rubber network are approximately orthogonal parameters, and that each can be optimized independently when designing miktoarm-based TPEs. Lastly, we show that this deflection of phase boundaries opens up large windows of parameter space where the Frank−Kasper phases σ and A15 are predicted to be stable.

METHODS

Miktoarm Model. We consider a neat incompressible melt of n_p $A_l(BA')_n$ miktoarm star polymers in volume V. Each miktoarm star polymer consists of l arms that are A homopolymers and n arms that are BA′ diblocks. The degree of polymerization of each of arm type is given by N_A and $N_{BA'} = N_B + N_{A'}$, respectively. The total degree of polymerization of a miktoarm star is, therefore, $N_t = lN_A + nN_{BA'}$ and the volume fraction of the A block is $f_A = (lN_A + nN_{A'})/N_t$. We define $N = N_A + N_{BA'}$, and note that N is unchanged when varying the number of arms n and l. This choice was made to be consistent with the phase diagrams of Lynd et al.[28] where results were presented in terms of $N_{ABA'} = N_A + N_{BA'}$. The bidispersity of the A and A′ blocks is represented by the block asymmetry parameter $\tau = N_A/(N_A + N_{A'})$.[19,34] For simplicity, we have assumed that A and B monomers have equal statistical segment lengths, $b \equiv b_A = b_B$, and that they occupy the same volume, v_0. All lengths were normalized by the unperturbed radius of gyration of a linear chain $R_g = \sqrt{b^2N/6}$.

By following standard procedures, a field-theory of this model (using notation of "model E" in ref 35) can be derived where the canonical partition function is given by

$$Z(n, N, T) = Z_0 \int \mathcal{D}w_+ \int \mathcal{D}w_- \exp(-H[w_+, w_-]) \tag{1}$$

$$H[w_+, w_-] = \rho_0 \int d\boldsymbol{r} \left[\frac{1}{\chi} w_-(\boldsymbol{r})^2 - i w_+(\boldsymbol{r}) \right] - n_p \ln Q[w_A, w_B] \tag{2}$$

where Z_0 contains the contribution from an ideal gas of miktoarm star polymers, the fields w_A, $w_B = iw_+ \mp w_-$, χ is the Flory−Huggins parameter that controls the interactions between A and B blocks, and $\rho_0 = v_0^{-1} = n_pN_t/V$ is the average monomer number density. All information about the polymer architecture and chain statistics are contained within $Q[w_A,w_B]$, the single-chain partition function. For the miktoarm architecture

$$Q[w_A, w_B] = \frac{1}{V} \int d\boldsymbol{r} \prod_{\upsilon} q_\upsilon(\boldsymbol{r}, N_\upsilon) \tag{3}$$

where the product runs over all $\upsilon = l + n$ arms in the miktoarm star, N_υ is the length of the υth arm, and the propagator, q_υ describes the probability of finding a monomer at spatial position $\boldsymbol{r}$ and contour position s, by propagating from the free end of the υth arm. For Gaussian chain statistics, $q_\upsilon(\boldsymbol{r},s)$ satisfies the modified diffusion equation

$$\frac{\partial}{\partial s} q_\upsilon(\boldsymbol{r}, s) = \frac{b^2}{6} \nabla^2 q_\upsilon(\boldsymbol{r}, s) - w_\upsilon(\boldsymbol{r}; s) q_\upsilon(\boldsymbol{r}, s) \tag{4}$$

with initial condition $q_\upsilon(\boldsymbol{r},0) = 1$, and $w_\upsilon(\boldsymbol{r};s) = w_K(\boldsymbol{r})$ if contour position s is a monomer of type K (for K = A or B). The complementary propagators, $q_\upsilon^\dagger(\boldsymbol{r},s)$, also satisfy eq 4 but are subject to the initial condition $q_\upsilon^\dagger(\boldsymbol{r},0) = \prod_{\mu\neq\upsilon} q_\mu(\boldsymbol{r},N_\mu)$, which reflect the constraint that all υ arms join together at the star center. The density operator is defined as

$$\tilde{\rho}_K(\boldsymbol{r}) = \frac{n_p}{VQ} \sum_\nu \int_{\Omega_K} ds q_\nu(\boldsymbol{r}, s) q_\nu^\dagger(\boldsymbol{r}, N_\nu - s) \tag{5}$$

where $\int_{\Omega_K} ds$ indicates an integration over all contour positions s within blocks of monomer type K (for K = A or B), and the volume fraction is given by $\phi_K(\boldsymbol{r}) = \tilde{\rho}_K(\boldsymbol{r})/\rho_0$.

Self-Consistent Field Theory. In SCFT the functional integral in eq 1 is assumed to be dominated by the inhomogeneous mean-fields $w_+^*(\boldsymbol{r})$ and $w_-^*(\boldsymbol{r})$. Under this approximation, the free energy, F, of a mean-field configuration is given by

https://dx.doi.org/10.1021/acs.macromol.9b02254
Macromolecules 2020, 53, 513−522

$$\frac{F}{k_B T} = -\log Z \approx H[w_+^*, w_-^*] \tag{6}$$

where w_+^* and w_-^* are saddle-points of H that satisfy

$$\left.\frac{\delta H[w_+, w_-]}{\delta w_+(\boldsymbol{r})}\right|_{w_+^*, w_-^*} = \left.\frac{\delta H[w_+, w_-]}{\delta w_-(\boldsymbol{r})}\right|_{w_+^*, w_-^*} = 0 \tag{7}$$

The fields w_+^* and w_-^* are solved using a steepest descent scheme with field updates performed using the semi-implicit Seidel scheme.[36] The modified diffusion equation was solved using a second-order operator splitting algorithm.[37]

Phase diagrams were constructed by computing the free energy of candidate phases at different model parameters (i.e., f_A, τ, l, n, χN), and drawing phase boundaries where the intensive free energies of two phases are equal. Additional details, including spatial and contour resolutions, are provided in the Supporting Information.

Field-Theoretic Simulation of B&M Phase. The B&M phase was formed using FTS of blends of $A(BA')_3$ miktoarms and the A homopolymer as described in previous work.[32] To numerically stabilize these calculations and to remove UV divergences, the model was adjusted from that described in eq 2 to include softer contact interactions by smearing particle centers with a Gaussian convolution of width a and permitting local deviations from the total density ρ_0 through the use of a Helfand compressibility.[38]

To compute the bridging statistics in the B&M phase, the fields from the FTS simulations were subsequently relaxed to a local saddle point using SCFT. Although the B&M phase spontaneously emerges only in the presence of fluctuations, we found that instantaneous snapshots of the B&M phase represent stable SCFT saddle points, and that this procedure resulted in an intact B&M morphology for the bridging analysis. Once the resulting w_+^* and w_-^* fields were obtained, they were used to calculate the bridging fraction as described in the following section.

For our calculations of the B&M phase, neat A(BA′)3 miktoarms with $f_A = 0.4$ and $\tau = 0.9$ were blended with homopolymers of length αN_t where $\alpha = 0.14$, with the homopolymer volume fraction given by ϕ_H. For these calculations $\chi N_t = 34$, the Helfand compressibility coefficient $\zeta N_t = 100$, the dimensionless chain number density $C = 20$ ($\bar{N} = 6^3 C^2$), the Gaussian smearing width $a = 0.2R_g$, and cell size is $101.7R_g \times 105.7R_g$ and a spatial resolution of 512×512 (simulations were conducted in two dimensions). Field updates were performed using the Euler−Maruyama predictor corrector method.[39]

Bridging. There are numerous examples in the literature for calculating the bridging statistics of linear block copolymers.[27,40] More recently, Spencer and Matsen have developed an elegant approach to calculate the bridging statistics of $(BA)_n$ stars consisting of n identical diblock arms.[41] The approach described here extends the work of Spencer and Matsen to account for the l homopolymer arms that compose the $A_l(BA')_n$ considered in our work.

The first step in computing bridging statistics is to define a region $\mathcal{R}$ within the simulation cell. This region $\mathcal{R}$ is defined using a converged density profile from SCFT, and is typically centered on a discrete A domain. For well-ordered symmetric morphologies (i.e., lamella, cylinders, spheres), all A domains are equivalent, and region $\mathcal{R}$ is defined by first performing a Voronoi tessellation using all A domain centers, and then defining $\mathcal{R}$ as one of these Voronoi cells. For other morphologies like the B&M phase or in Frank−Kasper phases, each A domain is not necessarily equivalent and it is necessary to define a different $\mathcal{R}$ for each A domain within the morphology. Furthermore, definition of region $\mathcal{R}$ for the B&M phase is complicated by the rough and asymmetric shape of A domains, which prevents the use of a simple Voronoi tessellation as in the symmetric morphologies. Our procedure for defining $\mathcal{R}$ for the B&M phase is described in the Supporting Information.

Once $\mathcal{R}$ is defined, the next step is to compute a modified propagator for the BA′ arms, $\bar{q}_{BA}(\boldsymbol{r},s)$, which corresponds to the propagator for an arm with its B−A′ junction constrained to $\mathcal{R}$. $\bar{q}_{BA}(\boldsymbol{r},s)$ is obtained by solving eq 4 with fields $w_\pm^*$, subject to the modified initial condition

$$\bar{q}_{BA}(\boldsymbol{r}, s = N_{A'}) = \begin{cases} q_{BA}(\boldsymbol{r}, s = N_{A'}) & \text{if } \boldsymbol{r} \in \mathcal{R} \\ 0 & \text{otherwise} \end{cases} \tag{8}$$

and propagating forward until $s = N_{BA'}$. As $\bar{q}_{BA}(\boldsymbol{r},s)$ is not periodic in space, it is necessary to perform this step using a large-cell simulation to remove finite size effects. In practice, this was achieved by periodically replicating the $w_\pm^*$ fields from the unit-cell calculations several times in each dimension prior to the calculation of $\bar{q}_{BA}(\boldsymbol{r},s)$.

Given $\bar{q}_{BA}(\boldsymbol{r},s)$, the single chain partition function of a $A_l(BA')_n$ miktoarm star centered at $\boldsymbol{r}$ with m arms in region $\mathcal{R}$ and $n - m$ arms outside of $\mathcal{R}$ is

$$Q_m(\boldsymbol{r}) = \binom{n}{m} \bar{q}_{BA}^m(\boldsymbol{r}, N_{BA'})[q_{BA}(\boldsymbol{r}, N_{BA'}) - \bar{q}_{BA}(\boldsymbol{r}, N_{BA'})]^{n-m} \times q_A^l(\boldsymbol{r}, N_A) \tag{9}$$

As explained by Spencer and Matsen,[41] the first factor is the number of ways of choosing m of the total n BA′ arms, the second factor is the partition function for m arms with their BA′ junction constrained to $\mathcal{R}$, and the third factor is the partition function for $n - m$ arms constrained to have their BA′ junction outside of $\mathcal{R}$. The final term is unique to our work and provides an additional constraint because of the l A homopolymer arms, where $q_A(\boldsymbol{r},N_A)$ is the unmodified single chain propagator. Upon normalization, we define the joint probability distribution

$$P_m(\boldsymbol{r}) = mQ_m(\boldsymbol{r})/Q' \tag{10}$$

where $P_m(\boldsymbol{r})$ gives the probability that an arm in $\mathcal{R}$ belongs to a star centered at position $\boldsymbol{r}$ that has a total of m arms in $\mathcal{R}$. The factor of m accounts for the multiplicity of star arms in $\mathcal{R}$. The normalization factor Q' is the partition function of a star with one or more arms in $\mathcal{R}$

$$\begin{aligned} Q' &= \int d\boldsymbol{r} \sum_{m=1}^{n} mQ_m(\boldsymbol{r}) \\ &= n \int d\boldsymbol{r} \bar{q}_{BA}(\boldsymbol{r}, N_{BA'}) q_{BA}^{n-1}(\boldsymbol{r}, N_{BA'}) q_A^l(\boldsymbol{r}, N_A) \end{aligned} \tag{11}$$

where the second line makes use of the binomial theorem and the identity $m\binom{n}{m} = n\binom{n-1}{m-1}$.

In the $A_l(BA')_n$ miktoarm stars considered here, each of the n BA′ arms in the star can either loop or bridge between region $\mathcal{R}$ and other A domains. This results in a distribution of different star configurations with different degrees of looping/bridging. For example, for $A(BA')_3$ stars, there can be one, two, or three BA′ arms in region $\mathcal{R}$, and the star center can either be in $\mathcal{R}$ or outside of $\mathcal{R}$, resulting in six possible chain configurations (see Figure S2). This distribution of chain configurations can be determined from $P_m(\boldsymbol{r})$ by calculating the integrated (or marginal) probability distribution, $\bar{P}_b$, of b arms bridging between region $\mathcal{R}$ and all regions other than $\mathcal{R}$

$$\bar{P}_b = \begin{cases} \int_{r\in\mathcal{R}} d\boldsymbol{r} P_{n-b}(\boldsymbol{r}) + \int_{r\notin\mathcal{R}} d\boldsymbol{r} P_b(\boldsymbol{r}) & b < n \\ \int_{r\notin\mathcal{R}} d\boldsymbol{r} P_b(\boldsymbol{r}) & b = n \end{cases} \tag{12}$$

Note that this equation accounts for the symmetry of equivalent miktoarm stars for both $\boldsymbol{r} \in \mathcal{R}$ and $\boldsymbol{r} \notin \mathcal{R}$ (Figure S2). Finally, the bridging fraction, ν_B, can be obtained by summing over all configurations with $b > 0$

$$\nu_B = \sum_{b=1}^{n} \bar{P}_b = 1 - \bar{P}_0 \tag{13}$$

where the final expression uses the fact that $\sum_{b=0}^{n} \bar{P}_b = 1$ and $\bar{P}_0$ is the fraction of miktoarm stars that form loops with all of their n BA′ arms.

https://dx.doi.org/10.1021/acs.macromol.9b02254
Macromolecules 2020, 53, 513−522

RESULTS

Phase Boundary Deflection. To examine the limits of phase boundary deflection that can be achieved with the $A(BA')_n$ miktoarm architecture, we begin by examining the cylinder/gyroid phase boundary for different values of τ and n for $\chi N = 40$ (Figure 1). The cylinder/gyroid phase boundary

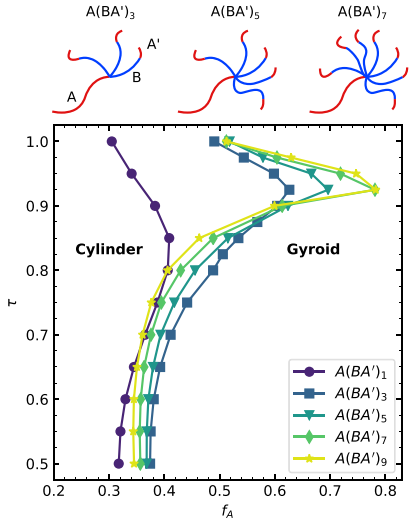

Figure 1. Cylinder-gyroid phase boundary as a function of block asymmetry parameter, τ, and block fraction, f_A, for $A(BA')_n$ miktoarm stars for $\chi N = 40$. For optimal choices of $\tau \approx 0.925$ and $n = 9$ the cylinder-gyroid phase boundary can be deflected to $f_A \approx 0.78$.

corresponds to a transition from discrete A domains (cylinders) to continuous A domains (gyroid), which induces a transition from elastic to brittle thermoplastic elastomers. Consistent with our prior work,[28] $A(BA')_3$ miktoarm stars achieve modest deflection of this phase boundary relative to ABA′ triblocks for all values of τ, shifting the maximum f_A at which cylinders can be achieved from 0.37 to 0.62. For increasing $n > 3$, however, the direction of phase boundary deflection exhibits a strong dependence on τ. For $\tau < 0.9$, increasing $n > 3$ results in deflection of the phase boundary to *decreased* values of f_A, with phase boundaries comparable to the linear ABA′ triblocks. When $\tau = 1.0$, the phase boundaries are approximately constant for all $n > 3$, indicating that the effect of AB_n miktoarm frustration on the deflection of phase boundaries has essentially saturated, as found previously for the AB_n limit.[12] However, for the narrow range of $0.9 < \tau < 0.975$, the deflection of the phase diagram to larger f_A is quite dramatic, with cylinders stable up to $f_A = 0.78$ for $A(BA')_9$.

Prior work by Matsen on ABA′ triblocks[19] and by our group on $A(BA')_3$ miktoarm stars[28] has argued that this optimal value of τ can be understood as a trade-off between bidispersity and A′ pull-out. The energetic benefits of bidispersity increase as τ approaches unity; as the A′ blocks become shorter and the A blocks grow longer (to maintain fixed f_A), the total chain stretching energy is decreased. This occurs because the bidisperse brush permits a larger fraction of A monomers to be far from the A−B interface, which results in a net decrease in chain stretching energy. Yet, when the A′ blocks become too short, they pull out and mix with the B domain, and the benefits of bidispersity are lost. The optimal value of $\tau = 0.925$ appears to strike a balance between these two competing effects, and results in significant deflection of the cylinder/gyroid phase boundary.

The balance between bidispersity and chain pull-out can be quantified by examining the bridging fraction, ν_B, as a function of τ in the cylindrical phase (Figure S3a). Increasing $\tau \gtrsim 0.9$ results in a rapid decrease in ν_B, which corresponds to the pull-out of the short A′ blocks. Notably, the pull-out of these A′ blocks is accompanied by a rapid increase in the domain spacing (Figure S3b), an effect first noted in linear ABA′ triblocks.[19] This occurs because the mixing of the extracted A′ blocks relieves the chain stretching in the B block, which stabilizes the microphase at larger domain spacings. Prior work by our group[28] noted that this rapid increase in domain spacing occurs approximately at the optimal value of τ, and our results presented here are consistent with this finding.

We next examine how such large values of f_A affect the appearance of the cylindrical phase (Figure 2). For moderate

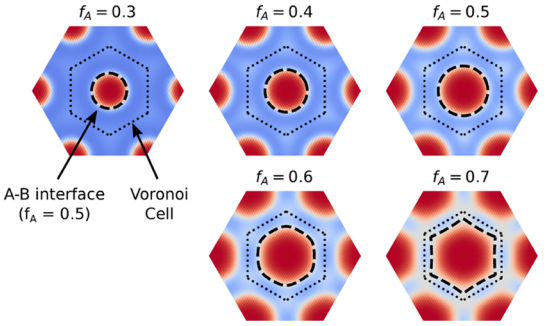

Figure 2. Density profiles of the cylindrical phase at increasing volume fraction, f_A. For moderate volume fractions $f_A = 0.3-0.5$, the A−B interface is smooth and cylindrical. For $A(BA')_7$ miktoarm stars, which stabilize the cylindrical phase up to $f_A > 0.6$, the A−B interface becomes faceted as the interface deforms to match the Voronoi cell of that domain. The plotted densities correspond to $A(BA')_9$ miktoarm stars with $\tau = 0.925$ and $\chi N = 40$. The dashed line denotes the contour where $f_A = 0.5$.

volume fractions $f_A = 0.3-0.5$, the diameter of the cylinder is small relative to the Voronoi cell of that cylinder, and the A−B interface is observed to be round and smooth. For larger volume fractions $f_A \geq 0.6$, the diameter of the cylinder approaches the size of the Voronoi cell, and the cylinders are observed to deform into faceted domains, where the A−B interface deforms to match the Voronoi cell of the cylindrical domain (in this case, to form a hexagon).

Prior work by Grason and Kamien has examined the transition from smooth to faceted interfaces as a shifting balance between regimes where either interfacial energy or chain stretching dominate.[12] When f_A is low, the stretching penalty incurred by the B chains to fill the Voronoi is relatively small and the interfacial energy dominates, which results in smooth A−B interfaces. The stretching penalty incurred by the B chains increases with f_A, which eventually leads to a cross-over where the chain stretching dominates relative to interfacial energy. Chain stretching favors interfaces that match those of the Voronoi cell, and this cross-over leads to the deformed domains that we observe in Figure 2.

The effects of τ and n are not unique to the cylinder/gyroid phase boundary, and are also observed to deform the phase boundaries between the sphere/cylinder and gyroid/lamellar phases (Figure 3). As with the cylinder/gyroid phase boundary discussed in Figure 1, the extent of phase boundary deflection

https://dx.doi.org/10.1021/acs.macromol.9b02254
Macromolecules 2020, 53, 513−522

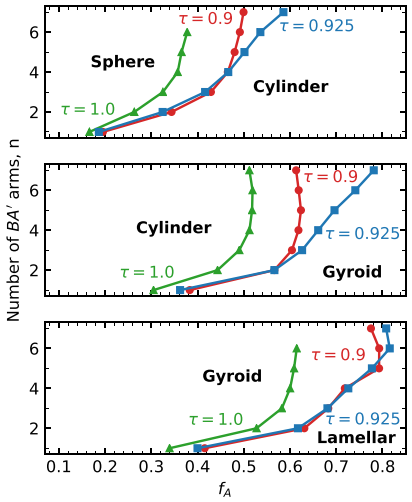

Figure 3. Phase boundary deflection with miktoarm architecture for classical phases (BCC spheres, hexagonal cylinders, double gyroid, and lamella). All phase boundaries deflect to larger f_A with increasing number of BA′ arms. Whereas phase boundary deflection in AB_n miktoarm stars (τ = 1.0) saturates by $n \approx 4$, the bidispersity effect of the small A′ blocks when τ = 0.9 and 0.925 permits continued phase boundary deflection up to n = 7. Simulations were performed at χN = 40.

is strongly dependent on τ. In the limit of τ = 1, the A′ blocks shrink to zero, and our miktoarm stars become the widely studied AB_n.[8−10,12−14] For these molecules, the phase boundary deflection saturates by $n \approx 4$, with only minor deflections for increasing number of arms. A choice of τ = 0.9 delays this saturation to slightly larger values of $n \approx 5$. However, for τ = 0.925 saturation is not observed for the sphere/cylinder and cylinder/gyroid phase boundaries up to n = 7. In this case, the additional BA′ arms result in a sphere/cylinder boundary at f_A = 0.68, and a gyroid/lamellar boundary f_A = 0.81, significantly higher values than observed for the widely studied AB_n miktoarm stars (f_A = 0.37 and f_A = 0.61, respectively). Note that this analysis was performed at χN = 40 and that different values of χN can have a significant effect on the locations of these phase boundaries (to be discussed in Figure 9). Nonetheless, these results indicate that the combination of bidispersity and miktoarm frustration present in the $A(BA')_n$ architecture interact cooperatively, and result in larger phase boundary deflections than could be achieved by either effect alone.

Whereas such deflection of phase boundaries is impressive, the ability to synthesize such precise miktoarm stars can be challenging in practice. For example, incomplete coupling reactions between the polymer arms and the star core[29,42] or arm dispersity[43] can result in a variable number of both A and BA′ arms, which could affect the deflection of phase boundaries discussed in Figure 3.

To examine if this is indeed the case, we have recomputed the cylinder/gyroid phase boundary for variations in both the number of A and BA′ arms, an architecture denoted by $A_l(BA')_n$ (Figure 4a). For increasing values of l, the extent of phase boundary deflection is significantly reduced. When l = 1, a deflection of the phase boundary to $f_A > 0.5$ requires only n = 2, whereas l = 2 requires n = 3 and l = 3 requires n = 5. Additional A arms counteract the induced curvature toward the A domains and favor flatter A−B interfaces, which retards the deflection of the phase boundaries with increasing n.

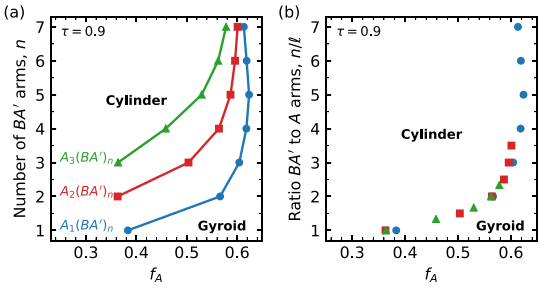

Figure 4. Effect of number of A homopolymer arms, l, on phase boundary deflection in $A_l(BA')_n$ miktoarm stars for τ = 0.9 and χN = 40. (a) As l increases, the deflection of phase boundaries is delayed to larger values of n. (b) Phase boundary deflection for $A_l(BA')_n$ miktoarm stars collapses to a single curve based on the ratio of n/l.

Notably, the phase boundaries for different values of l can be collapsed onto a single curve by plotting the ratio of BA′ arms to A arms or n/l (Figure 4). We note that our analysis here has assumed that $n > l$. Maintaining this equality is critical because if $n < l$, then the phase boundaries will be deformed in the *opposite* direction to that desired. Taken together, our results suggest that the ratio of A to BA′ arms is a critical parameter when designing miktoarm architectures that seek the maximum degree of phase boundary deflection. One promising synthetic approach that offers good control over this ratio is the recently developed μ STAR technique.[33]

Bridging. As discussed in the introduction, one possible application of the $A(BA')_n$ miktoarm design is for increasingly hard and tough thermoplastic elastomers (TPEs). Such materials can be achieved by taking advantage of the large phase boundary deflections discussed in Figure 1; the large values of f_A should result in materials with a high modulus, whereas the discrete A cylinder domains will maintain elasticity. The mechanical response of such materials will also be influenced by the configurations of the polymer chains themselves. Materials where a large fraction of the polymer molecules have their A and A′ blocks anchored in different glassy A domains (so-called bridging configurations) should be more robust mechanically than materials where most polymers' A and A′ blocks are anchored in the same domains (i.e., loops). We have developed an approach to calculate the prevalence of bridging configurations in melts of $A_l(BA')_n$ miktoarm stars (see methods), and employ it here to examine how the deflection of phase boundaries affects the propensity of miktoarms to bridge between different A domains.

We begin by calculating the spatial distribution $P_m(\boldsymbol{r})$ of $A(BA')_5$ miktoarm stars for the cylindrical morphology (Figure 5a−c). Recall that $P_m(\boldsymbol{r})$ is the probability of that an arm in $\mathcal{R}$ belongs to a star whose junction is at position $\boldsymbol{r}$ and has m arms in region $\mathcal{R}$. For stars with one arm in $\mathcal{R}$ (m = 1), the junction of these stars are located at the corners of the cylinders, which permits the miktoarm stars to bridge between multiple cylindrical domains (Figure 5a). When two or more arms are constrained in $\mathcal{R}$ ($m \geq 2$), the position of the stars is constrained to lie directly between two cylinders (Figure 5b,c).

The probability of each of these star configurations is quantified by the integrated probability distribution $\overline{P}_b$ of $A(BA')_n$ stars for n = 3, 5, 7 (Figure 5d). Recall that $\overline{P}_b$ is the probability that b of the total n arms bridge between different A domains, and that the distribution of $\overline{P}_b$ quantifies the prevalence of different looping and bridging star configurations

https://dx.doi.org/10.1021/acs.macromol.9b02254
Macromolecules 2020, 53, 513−522

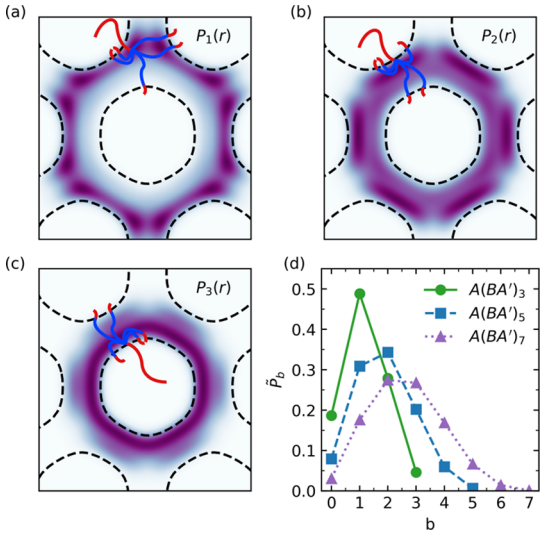

Figure 5. (a–c) Joint probability distribution, $P_m(\boldsymbol{r})$, of $A(BA')_5$ miktoarm stars centered at position $\boldsymbol{r}$ with one, two or three BA′ arms constrained to the central cylinder region $\mathcal{R}$. Dashed lines denote contours where $f_A = 0.5$. (d) Integrated probability distribution, $\bar{P}_b$, of b bridging arms for $A(BA')_3$, $A(BA')_5$, and $A(BA')_7$ miktoarm stars. For these calculations $f_A = 0.54$, $\chi N = 40$, and $\tau = 0.9$.

within a morphology (see Methods and Figure S2). As the number of BA′ arms increases, $\bar{P}_b$ broadens and shift to larger values, which indicates that an increase in n leads to an increase in the number of bridging arms between domains in the cylindrical network. For n = 3, 5, 7 the maxima occur at $\tilde{P}_b \approx \frac{n-1}{2}$, which suggests that combinatorial entropy is a dominant factor in dictating the distribution of bridging versus looping chains. However, as $\bar{P}_b$ is not symmetric about this maximum and the distribution skews toward higher values of b, our results suggest that bridging chains are slightly preferred to looping chains. We hypothesize that this results from the excluded volume of the arms, which favors bridging configurations as they relieve the steric congestion of the B monomer in the vicinity of the congested A–B interface. The trends seen in $P_m(\boldsymbol{r})$ and $\bar{P}_b$ for the cylindrical morphology are qualitatively similar to the BCC sphere and lamellar morphologies (Figures S4 and S5).

From $P_m(\boldsymbol{r})$ and $\bar{P}_b$, we can calculate the bridging fraction, ν_B, the probability that a miktoarm will bridge between two or more A domains (Figure 6). Consistent with prior work,[19,41] we have neglected the gyroid phase in this analysis. As the number of BA′ arms increase, ν_B increases for all values of f_A. For example, in the cylinder phase, the bridging fraction increases from 0.8 to 0.93 to 0.97 as n = 3, 5, 7. As shown previously,[19,41] the bridging fraction is strongly dependent on morphology, with discontinuous changes in bridging fraction at phase boundaries (shown by dotted lines in Figure 6). In the sphere phase, ν_B decreases slightly with f_A, whereas in the lamellar phase ν_B drops dramatically. The decrease in ν_B in the lamellar phase results from the rapid detachment of A′ blocks with small increases in f_A (see Figure S6). In the cylindrical phase, ν_B is approximately constant for all f_A, even up to large volume fractions of $f_A = 0.7$ for $A(BA')_5$. This result indicates that for the cylinder phase, phase boundary deflection can be achieved without sacrificing the bridging fraction, indicating that TPEs based on the miktoarm design should exhibit good

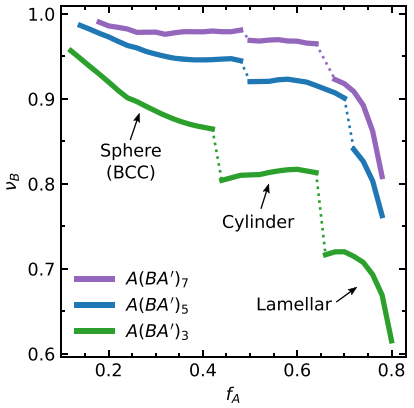

Figure 6. Bridging fraction, ν_B, as function of f_A for $A(BA')_3$, $A(BA')_5$, and $A(BA')_7$ miktoarm stars ($\tau = 0.9$, $\chi N = 40$). The bridging fraction increases significantly as the number of (BA′) arms increases. Dotted lines denote phase transitions. Note that the gyroid phase was neglected in this analysis.

mechanical properties even in the distorted cylinders shown in Figure 2.

A complimentary route for stabilizing discrete A domains at large values of f_A is through polymer alloys that form the B&M phase. These alloys consist of blends between cylinder-forming $A(BA')_3$ miktoarms with A homopolymers of a suitable molecular weight.[31] As the volume fraction of homopolymer ϕ_H is increased, the cylinders grow to accommodate the additional homopolymer, which eventually results in a fluctuation-induced phase transition to form the aperiodic B&M phase.[31,32]

Figure 7 shows how the bridging fraction ν_B changes with increasing ϕ_H. The spatial distribution of stars $P_1(\boldsymbol{r})$ is qualitatively similar between the hexagonal and B&M

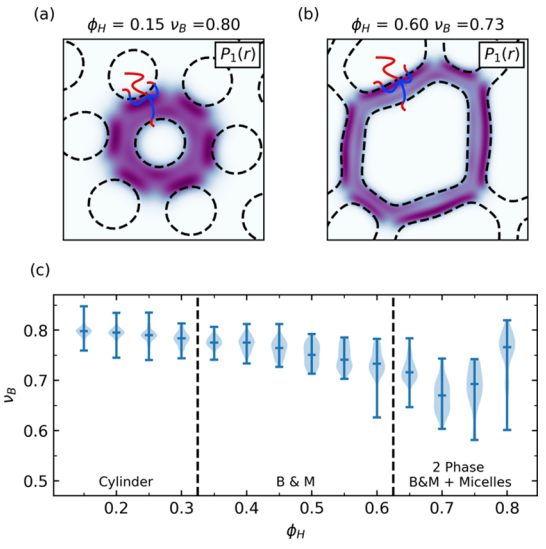

Figure 7. Bridging statistics for the B&M phase. (a) Joint probability distribution, $P_1(\boldsymbol{r})$, for the cylindrical phase. (b) Joint probability distribution, $P_1(\boldsymbol{r})$, for the B&M phase. (c) Violin plots indicate that the average bridging fraction is nearly unchanged as the homopolymer volume fraction, ϕ_H, is increased and the cylinder phase transitions to form the B&M phase. With the emergence of the B&M phase the distribution widens, indicating that the bridging fraction becomes increasingly heterogeneous throughout the sample. Vertical dotted lines denote phase transitions.

https://dx.doi.org/10.1021/acs.macromol.9b02254
Macromolecules 2020, 53, 513–522

morphologies, with the stars located along the domains adjacent to $\mathcal{R}$ (Figure 7a,b). As the cylindrical domains swell to form the B&M phase, the average bridging fraction decreases slightly from $\nu_B = 0.8$ for $\phi_A = 0.15$ to $\nu_B = 0.73$ for $\phi_A = 0.6$, in contrast to the discontinuous change in ν_B observed in other phase transitions (cf. Figure 6). This is consistent with our current understanding of the cylinder-B&M phase transition as a type of continuous unbinding transition.

As the B&M phase forms with increasing ϕ_H, the distribution of ν_B across the sample broadens as a consequence of heterogeneous structure of the B&M phase (Figure 7c). In these simulations, the large $101.7R_g \times 105.7R_g$ simulation cells consisted of 200−1000 discrete cylindrical or B&M domains and the distribution was obtained by selecting 50 domains at random. Despite the heterogeneous structure in the B&M phase, the average bridging fraction ν_B only changes slightly across $\phi_H = 0.15$−0.6. The relative insensitivity of ν_B with ϕ_H bodes well for the B&M phase as an approach to toughen TPEs by maintaining discrete A domains for large values of f_A.

Frank−Kasper Phases. As discussed in the introduction, phase boundary deflection is often accompanied by the emergence of new phases beyond the canonical BCC spheres, cylinders, double gyroid, and lamella. In particular, Grason and Kamien[12] and more recently Xie et al.[14] have shown that AB_n miktoarm stars can stabilize the Frank−Kasper sphere phases σ and A15. As our phase diagrams presented in Figure 3 indicate that $A(BA')_n$ miktoarm stars can stabilize spherical phases up to large f_A, we were curious if $A(BA')_n$ stars might also stabilize Frank−Kasper sphere phases.

To examine this possibility, we reconsidered the phase behavior of $A(BA')_7$ miktoarm stars with $\tau = 0.925$, which in Figure 3 exhibited the strongest phase deflection of the sphere/cylinder phase boundary of all miktoarm stars considered. We recomputed the free energies of the classical BCC and FCC sphere phases but now also considered the Frank−Kasper phases σ, A15, C14, and C15 (Figure 8a). This calculation

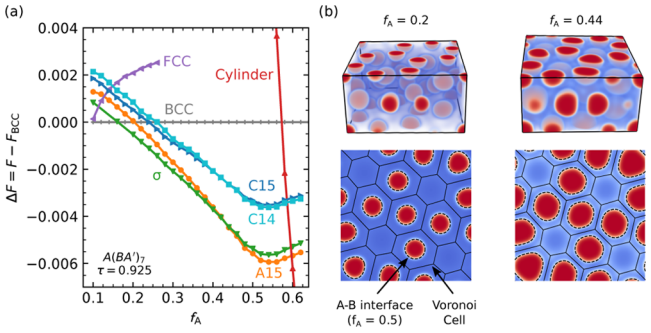

Figure 8. (a) Phase boundary deflection achieved with $A(BA')_7$ leads to the stability of the Frank−Kasper phases σ and A15 up to volume fractions $f_A = 0.45$ and $f_A = 0.59$, respectively ($\chi N = 40$). (b) The resulting σ phase at $f_A = 0.44$ exhibits domains that are faceted, and deform to match the Voronoi cell that constrains each domain.

indicates that the large sphere window that ranges from $f_A = 0.1$−0.59 is dominated by the σ and A15 phases, with only a miniscule region ($f_A = 0.1$−0.16) occupied by BCC spheres. Our results predict that the σ and A15 phases can be stabilized up to $f_A = 0.45$ and $f_A = 0.59$, respectively, values much larger than could be achieved with AB_n stars ($f_A = 0.3$, $f_A = 0.34$).[14] A consequence of the stability of σ and A15 at large f_A is that their domains begin to impinge on the Voronoi cell, which leads to a transition from a spherical A−B interface to one where the interface is deformed to match the Voronoi cell (Figure 8b).

In light of the large regions of σ and A15 stability, we computed the complete χN versus f_A phase diagram for $A(BA')_3$ and $A(BA')_5$ miktoarm stars (Figure 9). We observe

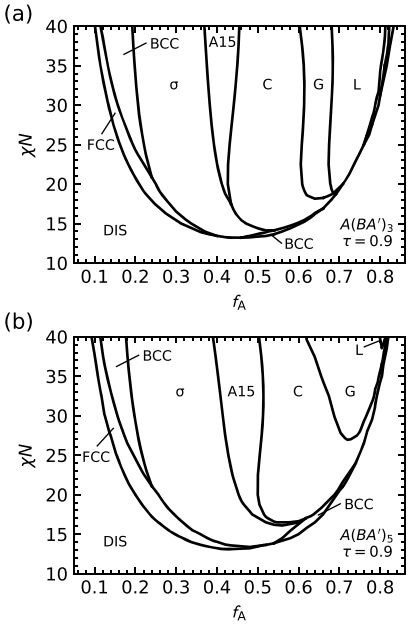

Figure 9. Phase diagrams of f_A vs χN for (a) $A(BA')_3$ and (b) $A(BA')_5$ miktoarm stars. Phase boundaries are deflected significantly to increased f_A and large regions of Frank−Kasper phases σ and A15 are stabilized.

large regions of stable σ and A15 phases that result from the large conformational asymmetry and the shift of phase boundaries to increased values of f_A. The shift of phase boundaries is particularly striking for $A(BA')_5$ miktoarm stars, which see a vanishingly small region of the lamellar phase that exists only at $f_A = 0.79$. An additional feature of these phase boundaries is the prevalence of many order−order transitions with changing χN. For example, σ transitions to cylinders along $f_A = 0.55$, and cylinders transition to gyroid along $f_A = 0.7$ (for $A(BA')_5$). We hypothesize that this phenomenon results from the bidispersity of the A and A′ blocks, which allows the A′ block to pull out and mix with the B phase at moderate χN. The balance between the enthalpic cost of A′ mixing with B and the release of chain-stretching in the B block results in order−order phase boundaries that depend on χN.

When analyzing the bridging statistics in Figure 6, we only considered the BCC sphere phase. Yet, our results in Figure 9 indicate that much of this region is dominated by other sphere phases like σ and A15. We were therefore interested in exploring how the bridging statistics vary across these different sphere phases and if some sphere phases might have properties that are superior to others.

In ordinary phases like cylinders and spheres, each domain is equivalent, and therefore the bridging fraction is the same for each domain. In Frank−Kasper phases, different micelles have different environments, which makes the bridging fraction dependent on their Wyckoff position. This is shown for the C15 phase (Figure 10a); the smaller micelles located at the

https://dx.doi.org/10.1021/acs.macromol.9b02254
Macromolecules 2020, 53, 513−522

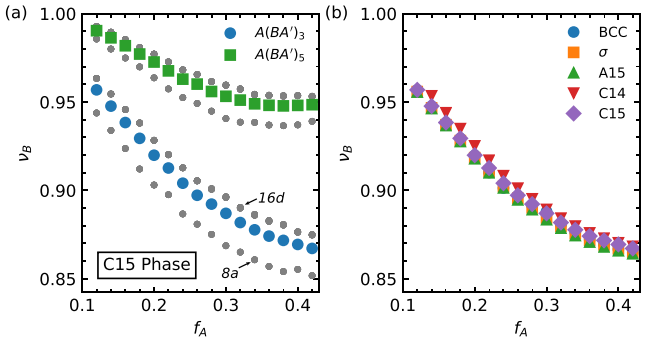

Figure 10. Bridging in Frank–Kasper sphere phases. (a) Bridging fraction of the C15 phase for $A(BA')_3$ and $A(BA')_5$ miktoarm stars. Micelles at the 8a and 16d Wycoff positions exhibit slightly different bridging fractions. (b) Bridging fraction for different Frank–Kasper phases for $A(BA')_3$ miktoarm stars. The bridging fraction is approximately the same for all sphere phases.

16d Wyckoff position have a slightly larger ν_B, whereas the large micelles at the 8a Wyckoff position have smaller ν_B. This is consistent with a general trend we observed for all sphere phases: the smaller a micelle, the larger that micelle's bridging fraction. We observe that the difference between the bridging fraction of the 8a and 16d micelles is relatively small, consisting of a difference in bridging fraction of less than 3%. The variations because of differences in micelle size have a slight impact of the average bridging fractions of different sphere phases (Figure 10b). We observe that the C14 phase exhibits the highest values of ν_B, whereas the A15 ν_B values are slightly lower. Nonetheless, these differences quite small and are all within 1% of the other sphere phases.

CONCLUSIONS

Here, we have shown that $A(BA')_n$ miktoarm stars can achieve considerable deflection of phase boundaries and can stabilize the σ and A15 Frank–Kasper phases across a wide range of f_A. The $A(BA')_n$ architecture achieves a much larger phase boundary deflection than the simpler AB_n architecture by combining miktoarm frustration and A block bidispersity to drive interfacial curvature toward the A domains. The stabilization of canonical phases up to large values of f_A results in an increasingly deformed A–B interface as the A domains begin to impinge upon the boundaries of their Voronoi cell. We have also shown that a critical parameter in $A(BA')_n$ miktoarm synthesis is the ratio of BA′ to A arms and that the deflection of phase boundaries observed here are only achieved if this ratio is sufficiently large.

An additional benefit of the $A(BA')_n$ architecture is that these molecules bridge between different A domains, which improves their mechanical response and makes them a promising candidate for hard, tough, and elastic TPEs. We have calculated the bridging statistics of these molecules, and show that the bridging fraction nearly unchanged as discrete A domains are stabilized with increasingly large f_A in both neat $A(BA')_n$ melts and in polymer alloys that form the "B&M" phase. This indicates that the increased modulus in TPEs that results from increased f_A is compatible with high levels of inter-domain bridging, both factors that are necessary to achieve distinguished TPEs.

Though our primary emphasis in this work was TPEs, there are numerous other application areas in which the $A(BA')_n$ design could prove to be useful. As the $A(BA')_n$ architecture can nearly decouple f_A from the resulting phase, we envision that the $A(BA')_n$ architecture could also be used in nanoporous membranes[44−46] where it is desirable to maintain a bicontinuous morphology (e.g., double gyroid), while simultaneously changing the volume fraction of the pores relative to the support (i.e., changing f_A). A similar approach could be applied to block polymer electrolytes, where recent work has indicated that polystyrene (PS) and poly(ethylene oxide) (PEO) $PS-PEO_3$ miktoarm stars exhibit higher ionic conductivity and modulus over linear PS–PEO analogues.[47] This work suggests that the miktoarm architecture leads to increased confinement of the PEO chains and lithium ions, which (for reasons not fully understood) leads to increased ionic conductivity. The $A(BA')_n$ design explored in our work here could provide a means to further enhance this intriguing effect.

ASSOCIATED CONTENT

Supporting Information

The Supporting Information is available free of charge at https://pubs.acs.org/doi/10.1021/acs.macromol.9b02254.

Additional details of bridging calculations, simulation parameters, analysis of chain pull-out, and additional bridging results (PDF)

AUTHOR INFORMATION

Corresponding Author

Glenn H. Fredrickson − *University of California, Santa Barbara, Santa Barbara, California;* orcid.org/0000-0002-6716-9017; Email: ghf@mrl.ucsb.edu

Other Authors

Joshua Lequieu − *University of California, Santa Barbara, Santa Barbara, California;* orcid.org/0000-0001-9480-0989

Trenton Koeper − *University of California, Santa Barbara, Santa Barbara, California*

Kris T. Delaney − *University of California, Santa Barbara, Santa Barbara, California;* orcid.org/0000-0003-0356-1391

Complete contact information is available at: https://pubs.acs.org/10.1021/acs.macromol.9b02254

Notes

The authors declare no competing financial interest.

ACKNOWLEDGMENTS

The authors thank Adam Levi, Christopher Bates, Doug Grzetic, Marc Charendoff, and Carl Willis for helpful discussions. This research was supported by the U.S. Department of Energy, Office of Basic Energy Sciences, under Award DE-SC0019001. Use was made of computational facilities purchased with funds from the National Science Foundation (CNS-1725797) and administered by the Center for Scientific Computing (CSC). The CSC is supported by the California NanoSystems Institute and the Materials Research Science and Engineering Center (MRSEC; NSF DMR 1720256) at UC Santa Barbara.

REFERENCES

(1) Bates, F. S.; Fredrickson, G. H. Block Copolymer Thermodynamics: Theory and Experiment. *Annu. Rev. Phys. Chem.* **1990**, *41*, 525−557.

(2) Bates, F. S.; Fredrickson, G. H. Block copolymers-designer soft materials. *Phys. Today* **1999**, *52*, 32−38.

(3) Leibler, L. Theory of Microphase Separation in Block Copolymers. *Macromolecules* **1980**, *13*, 1602−1617.

(4) Matsen, M. W.; Schick, M. Stable and unstable phases of a diblock copolymer melt. *Phys. Rev. Lett.* **1994**, *72*, 2660−2663.

(5) Huang, Y.-Y.; Hsu, J.-Y.; Chen, H.-L.; Hashimoto, T. Existence of fcc-packed spherical micelles in diblock copolymer melt. *Macromolecules* **2007**, *40*, 406−409.

(6) Tyler, C. A.; Morse, D. C. Orthorhombic Fddd network in triblock and diblock copolymer melts. *Phys. Rev. Lett.* **2005**, *94*, 208302.

(7) Takenaka, M.; Wakada, T.; Akasaka, S.; Nishitsuji, S.; Saijo, K.; Shimizu, H.; Hasegawa, H. Orthorhombic Fddd network in diblock copolymer melts. *Polym. Prepr. Japan* **2006**, *55*, 3113−3114.

(8) Matsen, M. W. Effect of architecture on the phase behavior of AB-type block copolymer melts. *Macromolecules* **2012**, *45*, 2161−2165.

(9) Hadjichristidis, N.; Iatrou, H.; Behal, S. K.; Chludzinski, J. J.; Disko, M. M.; Garner, R. T.; Liang, K. S.; Lohse, D. J.; Milner, S. T. Morphology and Miscibility of Miktoarm Styrene-Diene Copolymers and Terpolymers. *Macromolecules* **1993**, *26*, 5812−5815.

(10) Pochan, D. J.; Gido, S. P.; Pispas, S.; Mays, J. W.; Ryan, A. J.; Fairclough, J. P. A.; Hamley, I. W.; Terrill, N. J. Morphologies of Microphase-Separated A_2B Simple Graft Copolymers. *Macromolecules* **1996**, *29*, 5091−5098.

(11) Milner, S. T. Chain Architecture and Asymmetry in Copolymer Microphases. *Macromolecules* **1994**, *27*, 2333−2335.

(12) Grason, G. M.; Kamien, R. D. Interfaces in diblocks: A study of miktoarm star copolymers. *Macromolecules* **2004**, *37*, 7371−7380.

(13) Yang, L.; Hong, S.; Gido, S. P.; Velis, G.; Hadjichristidis, N. I_5S miktoarm star block copolymers: Packing constraints on morphology and discontinuous chevron tilt grain boundaries. *Macromolecules* **2001**, *34*, 9069−9073.

(14) Xie, N.; Li, W.; Qiu, F.; Shi, A. C. σ Phase formed in conformationally asymmetric AB-type block copolymers. *ACS Macro Lett.* **2014**, *3*, 909−910.

(15) Schulze, M. W.; Lewis, R. M.; Lettow, J. H.; Hickey, R. J.; Gillard, T. M.; Hillmyer, M. A.; Bates, F. S. Conformational Asymmetry and Quasicrystal Approximants in Linear Diblock Copolymers. *Phys. Rev. Lett.* **2017**, *118*, 207801.

(16) Bates, M. W.; Lequieu, J.; Barbon, S. M.; Lewis, R. M.; Delaney, K. T.; Anastasaki, A.; Hawker, C. J.; Fredrickson, G. H.; Bates, C. M. Stability of the A15 phase in diblock copolymer melts. *Proc. Natl. Acad. Sci. U.S.A.* **2019**, *116*, 13194−13199.

(17) Milner, S. T.; Witten, T. A. Bending moduli of polymeric surfactant interfaces. *J. Phys.* **1988**, *49*, 1951−1962.

(18) Milner, S. T.; Witten, T. A.; Cates, M. E. Effects of Polydispersity in the End-Grafted Polymer Brush. *Macromolecules* **1989**, *22*, 853−861.

(19) Matsen, M. W. Equilibrium behavior of asymmetric ABA triblock copolymer melts. *J. Chem. Phys.* **2000**, *113*, 5539−5544.

(20) Fredrickson, G. H.; Sides, S. W. Theory of polydisperse inhomogeneous polymers. *Macromolecules* **2003**, *36*, 5415−5423.

(21) Sides, S. W.; Fredrickson, G. H. Continuous polydispersity in a self-consistent field theory for diblock copolymers. *J. Chem. Phys.* **2004**, *121*, 4974−4986.

(22) Cooke, D. M.; Shi, A.-C. Effects of polydispersity on phase behavior of diblock copolymers. *Macromolecules* **2006**, *39*, 6661−6671.

(23) Lynd, N. A.; Hillmyer, M. A. Influence of polydispersity on the self-assembly of diblock copolymers. *Macromolecules* **2005**, *38*, 8803−8810.

(24) Lynd, N. A.; Hillmyer, M. A. Effects of Polydispersity on the Order-Disorder Transition in Block Copolymer Melts. *Macromolecules* **2007**, *40*, 8050−8055.

(25) Widin, J. M.; Schmitt, A. K.; Schmitt, A. L.; Im, K.; Mahanthappa, M. K. Unexpected consequences of block polydispersity on the self-assembly of ABA triblock copolymers. *J. Am. Chem. Soc.* **2012**, *134*, 3834−3844.

(26) Holden, G.; Legge, N.; Quirk, R.; Schroeder, H. *Thermoplastic Elastomers*, 2nd ed.; Hanser Publshers: Munich, 1996.

(27) Matsen, M. W.; Thompson, R. B. Equilibrium behavior of symmetric ABA triblock copolymer melts. *J. Chem. Phys.* **1999**, *111*, 7139−7146.

(28) Lynd, N. A.; Oyerokun, F. T.; O'Donoghue, D. L.; Handlin, D. L.; Fredrickson, G. H. Design of soft and strong thermoplastic elastomers based on nonlinear block copolymer architectures using self-consistent-field theory. *Macromolecules* **2010**, *43*, 3479−3486.

(29) Shi, W.; Lynd, N. A.; Montarnal, D.; Luo, Y.; Fredrickson, G. H.; Kramer, E. J.; Ntaras, C.; Avgeropoulos, A.; Hexemer, A. Toward strong thermoplastic elastomers with asymmetric miktoarm block copolymer architectures. *Macromolecules* **2014**, *47*, 2037−2043.

(30) Shi, W.; Hamilton, A. L.; Delaney, K. T.; Fredrickson, G. H.; Kramer, E. J.; Ntaras, C.; Avgeropoulos, A.; Lynd, N. A. Creating Extremely Asymmetric Lamellar Structures via Fluctuation-Assisted Unbinding of Miktoarm Star Block Copolymer Alloys. *J. Am. Chem. Soc.* **2015**, *137*, 6160−6163.

(31) Shi, W.; Hamilton, A. L.; Delaney, K. T.; Fredrickson, G. H.; Kramer, E. J.; Ntaras, C.; Avgeropoulos, A.; Lynd, N. A.; Demassieux, Q.; Creton, C. Aperiodic "Bricks and Mortar" Mesophase: a New Equilibrium State of Soft Matter and Application as a Stiff Thermoplastic Elastomer. *Macromolecules* **2015**, *48*, 5378−5384.

(32) Liu, Y.-X.; Delaney, K. T.; Fredrickson, G. H. Field-Theoretic Simulations of Fluctuation-Stabilized Aperiodic "bricks-and-Mortar" Mesophase in Miktoarm Star Block Copolymer/Homopolymer Blends. *Macromolecules* **2017**, *50*, 6263−6272.

(33) Levi, A. E.; Fu, L.; Lequieu, J.; Horne, J. D.; Blankenship, J.; Mukherjee, S.; Zhang, T.; Fredrickson, G. H.; Gutekunst, W. R.; Bates, C. M. Efficient Synthesis of Asymmetric Miktoarm Star Polymers. *Macromolecules* **2020**, DOI: 10.1021/acs.macromol.9b02380.

(34) Mayes, A. M.; Olvera De La Cruz, M. Microphase separation in multiblock copolymer melts. *J. Chem. Phys.* **1989**, *91*, 7228−7235.

(35) Fredrickson, G. *The Equilibrium Theory of Inhomogeneous Polymers*; Oxford University Press: Oxford, 2006.

(36) Ceniceros, H. D.; Fredrickson, G. H. Numerical Solution of Polymer Self-Consistent Field Theory. *Multiscale Model. Simul.* **2004**, *2*, 452−474.

(37) Rasmussen, K.; Kalosakas, G. Improved numerical algorithm for exploring block copolymer mesophases. *J. Polym. Sci., Part B: Polym. Phys.* **2002**, *40*, 1777−1783.

(38) Delaney, K. T.; Fredrickson, G. H. Recent Developments in Fully Fluctuating Field-Theoretic Simulations of Polymer Melts and Solutions. *J. Phys. Chem. B* **2016**, *120*, 7615−7634.

(39) Düchs, D.; Delaney, K. T.; Fredrickson, G. H. A multi-species exchange model for fully fluctuating polymer field theory simulations. *J. Chem. Phys.* **2014**, *141*, 174103.

(40) Drolet, F.; Fredrickson, G. H. Optimizing chain bridging in complex block copolymers. *Macromolecules* **2001**, *34*, 5317−5324.

(41) Spencer, R. K. W.; Matsen, M. W. Domain Bridging in Thermoplastic Elastomers of Star Block Copolymer. *Macromolecules* **2017**, *50*, 1681−1687.

(42) Avgeropoulos, A.; Hadjichristidis, N.; Copolymer, S. B. Synthesis of Model Nonlinear Block Copolymers of $A(BA)_2$, $A(BA)_3$, and $(AB)_3A(BA)_3$ Type. *J. Polym. Sci., Part A: Polym. Chem.* **1997**, *35*, 813−816.

(43) Levi, A. E.; Lequieu, J.; Horne, J. D.; Bates, M. W.; Ren, J. M.; Delaney, K. T.; Fredrickson, G. H.; Bates, C. M. Miktoarm Stars via Grafting-Through Copolymerization: Self-Assembly and the Star-to-Bottlebrush Transition. *Macromolecules* **2019**, *52*, 1794−1802.

https://dx.doi.org/10.1021/acs.macromol.9b02254
Macromolecules 2020, 53, 513−522

(44) Zalusky, A. S.; Olayo-Valles, R.; Wolf, J. H.; Hillmyer, M. A. Ordered nanoporous polymers from polystyrene-polylactide block copolymers. *J. Am. Chem. Soc.* **2002**, *124*, 12761−12773.
(45) Ndoni, S.; Vigild, M. E.; Berg, R. H. Nanoporous Materials with Spherical and Gyroid Cavities Created by Quantitative Etching of Polydimethylsiloxane in Polystyrene-Polydimethylsiloxane Block Copolymers. *J. Am. Chem. Soc.* **2003**, *125*, 13366−13367.
(46) Li, L.; Szewczykowski, P.; Clausen, L. D.; Hansen, K. M.; Jonsson, G. E.; Ndoni, S. Ultrafiltration by gyroid nanoporous polymer membranes. *J. Membr. Sci.* **2011**, *384*, 126−135.
(47) Lee, D.; Jung, H. Y.; Park, M. J. Solid-State Polymer Electrolytes Based on AB_3-Type Miktoarm Star Copolymers. *ACS Macro Lett.* **2018**, *7*, 1046−1050.

NOTE ADDED AFTER ASAP PUBLICATION

Due to production error, ref 33 was inadvertently omitted in the version published on January 8, 2020, and has been correctly restored on January 17, 2020.

https://dx.doi.org/10.1021/acs.macromol.9b02254
Macromolecules 2020, 53, 513−522